Aspect-Ratio Effects for Low-Order Modeling of Swept-Wing Stall

Abhimanyu Jamwal*, Pranav Hosangadi†, and Ashok Gopalarathnam‡
Dept. of Mechanical and Aerospace Engineering,
North Carolina State University, Raleigh, NC 27695-7910

Low-order decambering methods can be extended to swept wings by including the effects of spanwise transport of the separated boundary layer by modifying the viscous input curves provided to the methods. Modeling this effect without the use of pre-existing CFD solutions is an important step for a predictive low-order method. In this work, computational results are used to study the variation of the separation characteristics for varying sweeps and aspect ratios. Using a previously identified parameter α_s, regions of root-influence with delayed separation, and sweep-influence with advanced separation are identified. It is seen that the location of the boundary between these regions is independent of sweep and aspect ratio. The variation of separation characteristics in the region of advanced separation can be condensed to a linear curve depending only on sweep. No such trends were observed in the region of delayed separation. Using these observations, sectional characteristic curves can be created for arbitrary aspect ratios and sweep angles. The low order method yields sufficiently accurate lift and moment results using these characteristics. The methodology can also be applied to wings with more complicated planforms, such as a partially swept wing, by combining the spanwise variations observed for the rectangular and swept wings.

I. Introduction

Low-order aerodynamic prediction methods, such as lifting line theory, vortex lattice method (VLM) etc. are known to work well in the "linear regime" of aerodynamics, in which transport aircraft operate most of the time. In this region, the boundary layer stays largely attached to the lifting surface and these potential-flow-based methods successfully predict the lift and induced drag behavior of wings at low angles of attack. These methods tend to break down as the angle of attack increases into the "non-linear" regime, characterized by thick, separated boundary layers. This is because potential flow ignores viscosity, making it unsuitable for predictions at high angles of attack where viscous effects are dominant.

Extensive research has been conducted to extend potential-flow methods into the non-linear regime by modifying the potential-flow equations to model the effects of thick boundary layers and separated flow [1–8]. One such method, the decambering method [6, 9] developed at NCSU, uses a strip-theory approach to simulate separated flow with an effective reduction in the camber of the sections of the wing. For each section, viscous input data in the form of airfoil lift, moment, and separation curves (characteristics) are supplied and used as convergence criteria, while solving the governing equations of the 3-D potential flow to account for spanwise variation of lift. The decambering method produces sufficiently accurate results for rectangular and tapered wing geometries. However, attempting to model the stall of swept wings by this approach yields poor results. The presence of a spanwise pressure gradient on swept wings causes spanwise transport of the separated boundary layer from root to tip. This separated boundary-layer transport affects the viscous operating curves of the sections in a swept wing. Compared to the airfoil, sections near the root experience attached flow upto higher angles of attack, thereby undergoing delayed stall, whereas tip sections experience separation at lower angles of attack, and stall sooner [10].

Hosangadi et al. [11] prescribed a methodology to obtain modified viscous characteristic curves for swept-wing sections that account for separated boundary-layer transport from RANS CFD results, and demonstrated that these curves can be used with the decambering method to yield satisfactory results for swept wings. Figure 1 shows the variation of the separation point location, f, with the effective angle of attack of the section, α_{eff}, for a rectangular and swept wing at different sections across the span. The effects of sweep on separation behavior are evident – all sections

*Graduate Student, ajamwal@ncsu.edu
†Graduate Research Assistant, phosang@ncsu.edu. Student Member, AIAA
‡Professor, agopalar@ncsu.edu. Associate Fellow, AIAA

of the rectangular wing resemble the behavior of the airfoil whereas a significant difference is seen in the behavior of inboard and outboard sections of the swept wing. The modified viscous curves used in Ref. [11] were derived from the separation behavior of the sections, extracted from a database of RANS CFD results [12] for NACA 4415 wings with $\mathcal{R} = 12$ and varying angles of sweep.
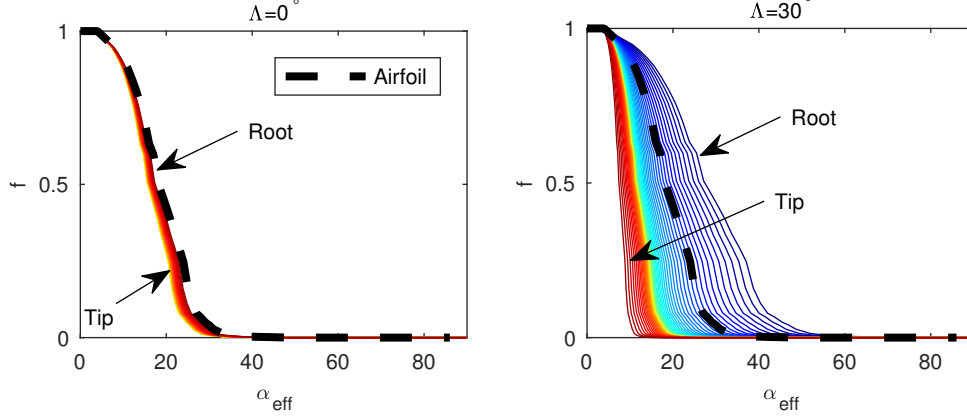
Fig. 1 **Separation behavior of the rectangular and** $30°$ **swept wings**

The current work aims to characterize the effects of aspect ratio on the spanwise transport of the separated boundary layer on swept wings by studying the variation in separation behavior, and to quantify the effects of aspect ratio on the extents of the root-influence and sweep-influence regions and the separation behavior in those regions. A newly developed database of RANS CFD solutions for NACA 4415 wings with $\mathcal{R} = 8$ and 16 is used to obtain the sectional separation behavior. The trends observed in the $\mathcal{R} = 8, 16$ wings are used to predict the separation behavior of $\mathcal{R} = 12$ wings. Finally, the suitability of this methodology to wings of more complicated planforms is demonstrated on a part-rectangular, part-swept wing.

II. Background

The decambering method developed at NCSU models the effects of a separated boundary layer with an effective reduction in camber. This method can be used to augment an inviscid panel method, such as the VLM, to predict the loss of lift at high angles of attack. The geometry is discretized into quadrilateral panels distributed on the camberline of the surface. Each panel consists of a vortex ring, placed such that the leading segment of the ring is at the quarter-chord point for the panel. A collocation point is defined at the three-quarter-chord point of the panel to enforce the boundary condition of zero normal flow. This system can be described by a set of linear equations which yield the circulation strengths of the vortex rings.

$$[AIC]\,\boldsymbol{\Gamma} + \boldsymbol{w} + \boldsymbol{w_{dec}} = 0 \tag{1}$$

Here, $\boldsymbol{\Gamma}$ is a column vector of the circulation strengths of the vortex rings, and $\boldsymbol{w}$ is a column vector of the normal components of all velocities except those induced by the geometry and wake. $\boldsymbol{w_{dec}}$ is a column vector of the velocities induced by the decambering.

The force on the ith panel is calculated using the Kutta-Joukowski theorem on its bound segment.

$$\vec{F}_i = \rho \vec{V}_i \times \vec{\Gamma}_i \tag{2}$$

The force on each chordwise row of panels is added to obtain the lift generated by the section. The operating point of the section can be found using the C_l and α_{eff} of the section.

$$C_l = \frac{2|\vec{F}_{lift}|}{\rho V_\infty^2 S_{strip}} \tag{3}$$

$$\alpha_{\text{eff}} = \frac{C_l}{2\pi} + \alpha_{0L} \tag{4}$$

2

In addition to the discretization, each section is assigned viscous C_l vs α, C_m vs. α, and f vs α curves to be used as the target for convergence by the decambering method.

The decambering method uses a strip-theory approach, in which the operating point for each section of the wing must fall on the viscous curve of that section for convergence. The variant of decambering used in this work is called nonlinear decambering, and was originally developed by Narsipur et al. [13] for 2D unsteady airfoil predictions. A quadratic flap hinged at the separation point provides the drop in lift required to model viscous behavior. Every section has three decambering variables – the location of the separation point, f; the angle of the decambering flap at the hinge, δ_l; and the height of the flap above the trailing-edge, m. Given the f location and the target C_l and C_m values, the values of δ_l and m are calculated using equations derived from thin airfoil theory.

Initially, decambering is assumed to be zero for all sections ($\delta_l = m = 0$). This corresponds to the inviscid-flow solution. For a pre-stall case, the inviscid solution (without decambering) lies on the viscous operating curve and no decambering is necessary. For higher angles, the inviscid solution predicts a higher lift than the viscous solution. A target C_l and C_m is identified by interpolating the lift and moment curves at the effective angle of attack of the section. The separation location for the section is interpolated from its f vs α_{eff} curve. The decambering variables δ_l and m are obtained for each section using Equation (5)

$$
\begin{bmatrix} \Delta C_l \\ \Delta C_m \end{bmatrix} = \begin{bmatrix} a_1 & b_1 \\ a_2 & b_2 \end{bmatrix} \begin{bmatrix} p_1 & q_1 \\ p_2 & q_2 \end{bmatrix}^{-1} \begin{bmatrix} \Delta m \\ \Delta \delta_l \end{bmatrix}
\tag{5}
$$

where

$$a_1 = 3\theta_f - 3\pi - 4\sin\theta_f + \frac{\sin 2\theta_f}{2} \qquad a_2 = \frac{3\sin\theta_f}{4} - \frac{3\sin 2\theta_f}{8} + \frac{\sin 3\theta_f}{12} - \frac{\theta_f - \pi}{4}$$

$$b_1 = 2(\theta_f - \pi - \sin\theta_f) \qquad b_2 = \frac{\sin\theta_f}{2} - \frac{\sin 2\theta_f}{4}$$

$$p_1 = (1-f)^2 + 2f(1-f) \qquad p_2 = 2f$$

$$q_1 = (1-f) \qquad q_2 = 1$$

and θ_f is the angular location of the separation location, given by

$$\theta_f = \cos^{-1}(1 - 2f)$$

The normal vectors for panels aft of the separation location are rotated by slope of the decambering line at the panel collocation point and the circulation strengths of the vortex rings are calculated. The lift at each section is affected by its own decambering and the decambering of every other section. This process is repeated until a set of decambering variables is obtained such that each section reaches its target C_l and C_m. Figure 2 shows an example of the nonlinear decambering flap for a NACA 4415 airfoil.
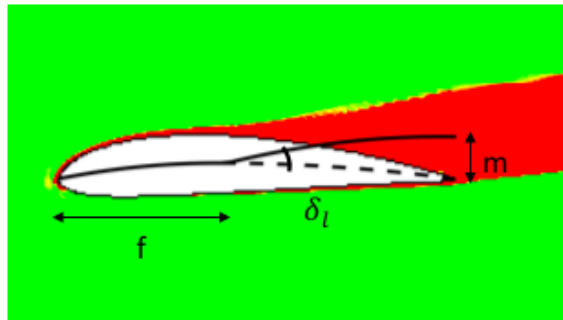

Fig. 2   Separated flow over a NACA4415 airfoil at high α, with the decambered camberline and nonlinear decambering variables.

III. Overview of Current Research

Readily available viscous lift and separation curves for the airfoil are sufficient to predict the forces on unswept geometries. To account for the effects of sweep, the spanwise pressure gradient and its effect on the section separation characteristics must be considered. Specifically, we need to account for the delayed separation at the wing root and the advanced separation at the wingtip. The separation characteristic curves for each section are first obtained by post-processing CFD solutions. This is depicted in Figure 3 with blue circles. Next, the separation curve of the airfoil, $f(\alpha)$, is transformed using Equation (6) to obtain the best fit, $f(\alpha_{new})$, with the section separation curve.

$$\alpha_{new} = \alpha_1 + \frac{\alpha_s - \alpha_1}{\alpha_a - \alpha_1}(\alpha - \alpha_1) \tag{6}$$

where α_1 is the angle of attack at which the flow on the airfoil just starts separating, α_a is the angle of attack where separation reaches 50% of the chord on the airfoil. The scaling factor, α_s, represents the effective angle of attack of the section at which the separation reaches 50% of chord, and can be considered the representative quantity for the separation behavior of the section. A high α_s indicates that the flow stays attached until a higher angle of attack. For a given airfoil, α_1 and α_a are constant. The transformed curve for the section is now given by $f(\alpha_{new})$, and is depicted with a red line in Figure 3. The transformed curve closely matches the actual separation characteristic of the section, and can be used in its place.
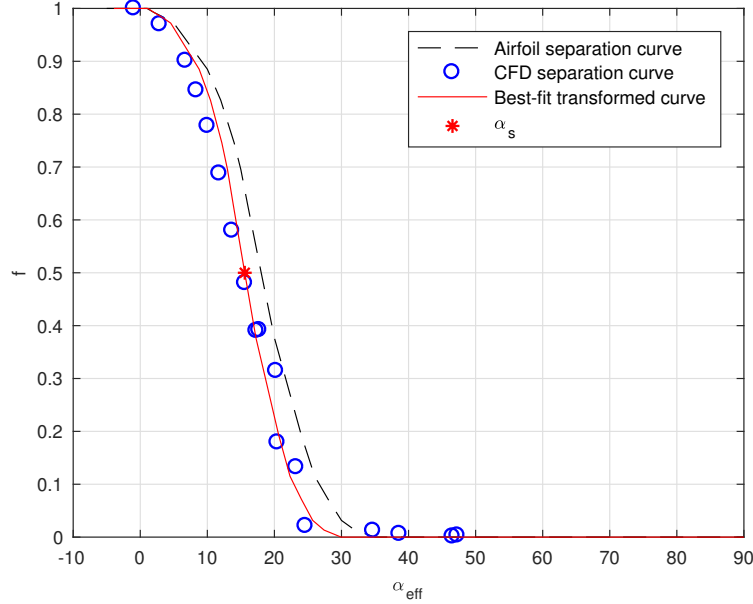

Fig. 3   Separation characteristic for a section of a swept wing.

Figure 4 shows the variation of α_s for wings of $\mathcal{R} = 12$ and different sweep angles. The α_s does not vary significantly across the span for the rectangular wing. This lack of variation is expected, and indicates that the separation behavior of the sections of a rectangular wing is similar across the span. Now, three distinct regions can be identified on the $\mathcal{R}12$ wings from Figure 4: Region A, where the boundary layer is primarily affected by the wing root and experiences delayed separation compared to the rectangular wing; Region B, where the effects of wing sweep are dominant, and separation is advanced compared to the rectangular wing; and Region C, where the effects of the wingtip vortex affect the separation behavior. Region C is ignored in this work.

IV. CFD Methodology

The CFD database of NACA 4415 wings with $\mathcal{R} = 12$ and quarter-chord sweep angles of $0°$, $10°$, $20°$, and $30°$ was generated by Petrilli et al. [12] using NASA's TetrUSS CFD software package and validated with experimental data available in the literature. The current work uses ANSYS ICEM-CFD for grid generation and ANSYS FLUENT as the
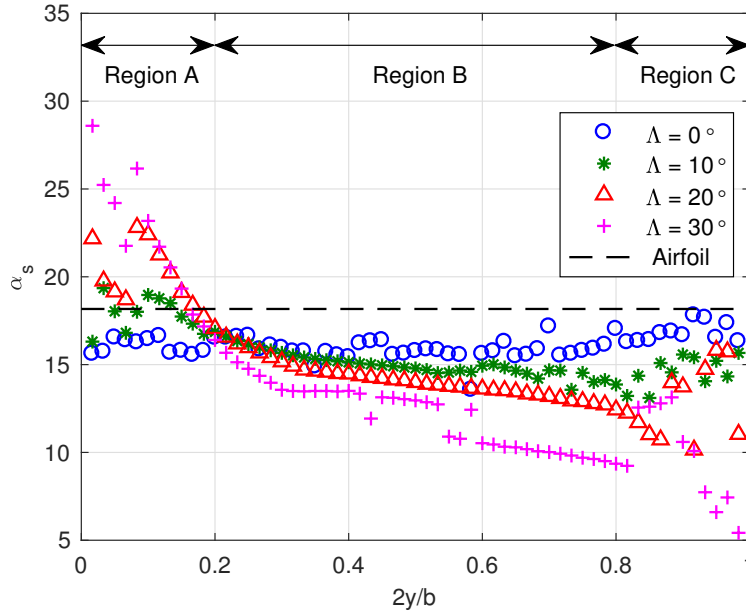
Fig. 4 Variation of α_s with non-dimensional spanwise coordinate (2y/b) for $\mathcal{R} = 12$, $\Lambda = 0°, 10°, 20°,$ and $30°$

flow solver. The numerical solver was tuned by validating the force and moment coefficients obtained with those from TetrUSS along with flow visualization of wing surface streamlines. Once the solver parameters were established, an efficient process to go from CAD geometry to a converged time-accurate flow solution was developed and is discussed in the following sections.

A. Geometry

The current work uses a modified NACA 4415 airfoil profile generated by Petrilli. The sharp-trailing edge NACA profile was modified by removing the aft 1% of chord perpendicular to the camber line, and the resultant profile was scaled up to a chord length of 1m. The wing geometries studied include the constant-chord modified NACA 4415 wing with $\mathcal{R} = 8$ and $\mathcal{R} = 16$ with quarter-chord sweep from $0° \leq \Lambda \leq 30°$ at intervals of $10°$.
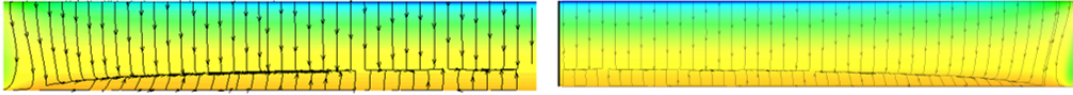
B. Grid Generation

The computational grids for this study were generated using the ANSYS ICEM-CFD tool. A body-conforming structured meshing approach, utilizing Multi-Blocking HEXA Algorithm, was used to gain control over the distribution of mesh points in the computational domain. The domain is composed entirely of hexahedral elements. All wings were simulated in the semi-span configuration with a symmetry plane at the root. A typical C-Grid topology was used for the URANS simulations with the inlet and outlet boundaries 20 chord lengths away from the wing and the side boundary at a distance of three semi-spans from the symmetry plane. In order to examine the grid sensitivity of the numerical solutions based on Richardson's Extrapolation method, a series of grids, by increasing surface and volume density by a factor of ~ 1.5 and varying cell densities and grid spacings, as shown in Table 1, were studied for the $\mathcal{R} = 12$ rectangular wing and 30° swept wing, The numerical solutions were compared with the TetrUSS results along with flow-visualization of skin-friction lines, as seen in Figure 5 and Figure 6. The 'Medium' grid specifications were deemed a reasonable compromise between the number of cell elements, computational time and numerical accuracy. The following parameters were used:

- Wall $Y^+ \leq 1$, leading to outward normal dimensional spacing of $\Delta_1 = 8.5 \, \mu m$
- Near-field growth rate and edge sizing = 1.1 with 150 grid points in outward normal direction from surface
- Far-field growth rate = 2
- Leading and trailing edge spacing = 0.3% of local chord
- Spanwise spacing = 0.1% semispan at root and tip

- Airfoil surface points = 360

**Table 1   Grid-sensitivity study parameters**

Grid Type and Parameters	Coarse	Medium	Fine
Wall Y^+	1	1	1
Near-Field Growth Rate and Edge-Sizing	1.1 , 100	1.1 , 150	1.1 , 175
Far-Field Growth Rate	2	2	2
Leading and Trailing Edge Spacing (% of local-chord)	0.5	0.3	0.1
Spanwise Spacing (% of semi-span at root and tip)	1.5	1	0.5
Airfoil Surface Points	220	360	500
Grid Size	$\approx$ 16 million	$\approx$ 31 million	$\approx$ 46 million

Fig. 5 C_P contours and skin-friction lines on a rectangular wing at $\alpha = 14°$, $\mathit{Æ}$ = 12, NACA 4415 airfoil, Re = 3 million - (a) ANSYS FLUENT solution (left side of wing), (b) TetrUSS solution (right side of wing).

This method of grid generation was applied to all wing geometries resulting in grids ranging from ~21 million ($\mathit{Æ}$ = 8) to ~40 million ($\mathit{Æ}$ = 16) hexahedral cells. For airfoil calculations, a 2D grid was generated using the same grid guidelines to maintain similar grid density between the wing grids and airfoil grids. Hence, a cut-section of any 3D wing grid resembles the airfoil grid completely. Figure 7 shows an illustration of the block-structured mesh topology and resolution of the grids used in this computational study.
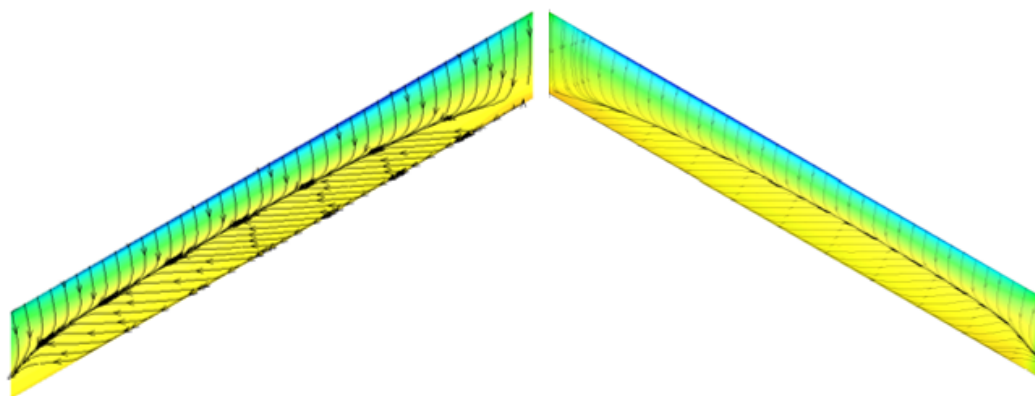
Fig. 6 C_P **contours and skin-friction lines on a** $30°$ **swept wing at** $\alpha = 16°$ **,** $Æ\!R$ **= 12, NACA 4415 airfoil, Re = 3 million - (a) ANSYS FLUENT solution (left side of wing), (b) TetrUSS solution (right side of wing).**


(a) Wing Leading Edge

(b) Wing Leading Edge-Symmetry Plane Junction

(c) Airfoil section cut

(d) Near-and Far-field regions
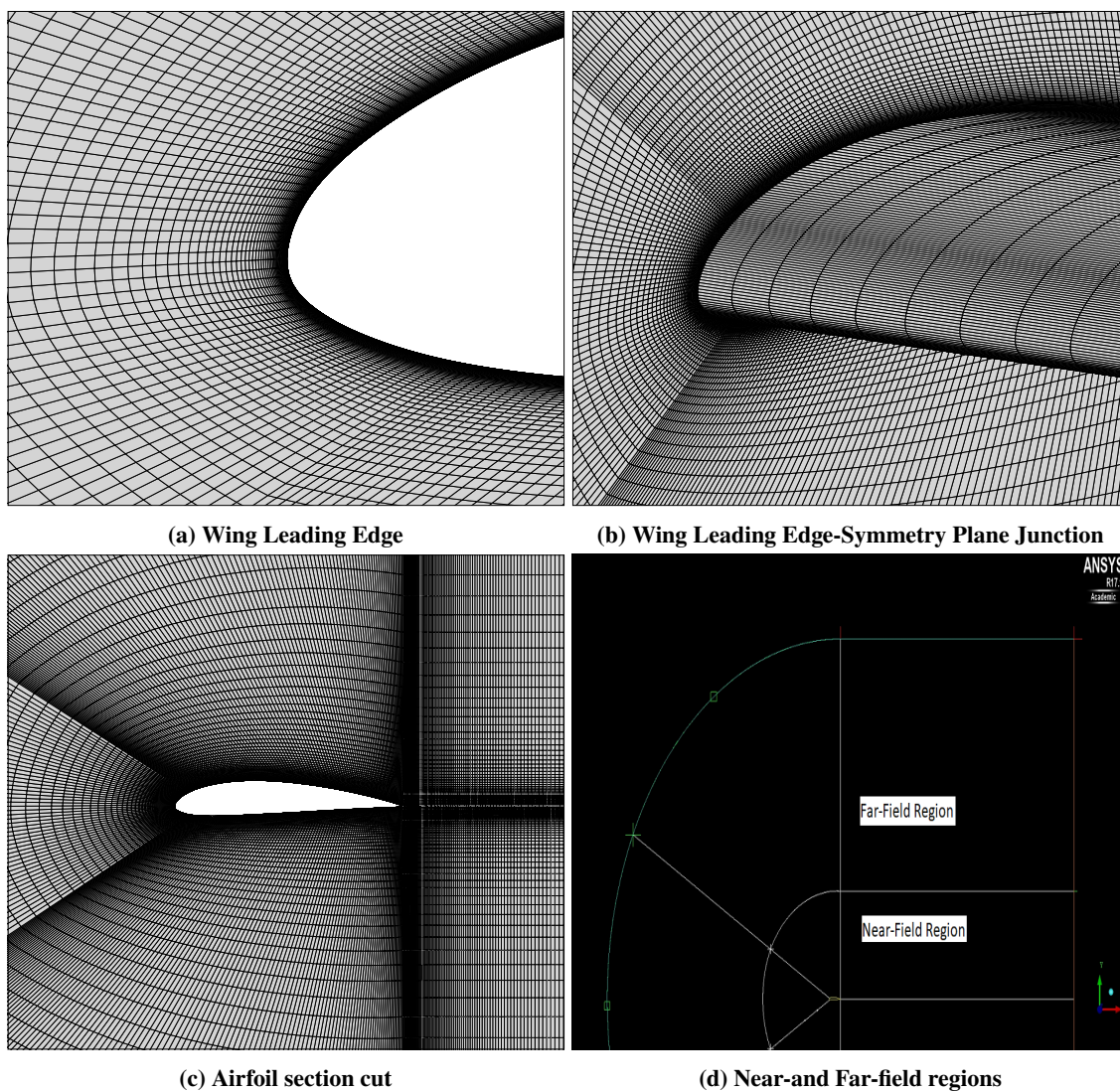
Fig. 7   Illustration of block-structured mesh topology for Blunt TE-NACA 4415 profile

C. Numerical Solver and Post-Processing

The flow solutions are developed using the ANSYS FLUENT commercial package, an unstructured, finite-volume method based CFD code. The incompressible Navier-Stokes equations are solved since the Mach number of the flow is low with a Reynolds number of 3 million. A pressure-based solver that solves the continuity, momentum, and turbulence equations in double precision is used. The COUPLED algorithm is used for pressure-velocity coupling. The temporal term is discretized with a second-order implicit scheme and the solution advanced with a physical time step size of 0.01s for a total of 300 steps. The number of sub-iterations for each time step was set between 20-40 to ensure adequate sub-iteration convergence. The convective and diffusive terms in the URANS equations are discretized with a second-order upwind scheme. The Spalart-Allmaras (SA) one equation turbulence model was used exclusively, maintaining continuity with TetrUSS solutions. The convergence criteria were set to 1e-5 for all residuals. The solver was run on the North Carolina State University High Performance Computing (NCSU HPC) cluster using 20-64 cores for 3D simulations. The solution files were processed using a combination of MATLAB scripts and Tecplot 360 macros.

V. CFD Results for $\mathcal{R} = 8$ and 16 Wings

The flow solutions obtained from CFD were post-processed to obtain the variation of α_s with spanwise location. This variation is presented here for the $\mathcal{R} = 8$ and $\mathcal{R} = 16$ wings. The same three regions observed in Ref. [11] and discussed in Section III for $\mathcal{R} = 12$ are seen.

(a) $\mathcal{R} = 8$ **(b)** $\mathcal{R} = 16$
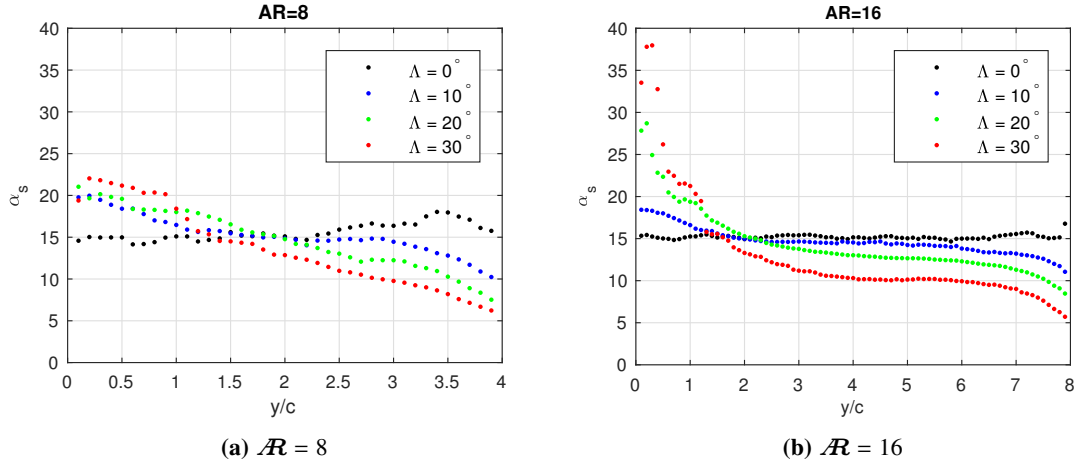
Fig. 8   Spanwise variation of α_s with y/c for $\Lambda = 0°, 10°, 20°,$ and $30°$ swept wings

A. Region A

Region A denotes the region near the wing root where boundary-layer separation is delayed by the spanwise pressure gradient. There is a sharp drop in α_s as we move out from $y/c = 0$, until α_s becomes equal to the α_s for the rectangular wing (α_s^{rect}) at the end of Region A. Figure 8 shows that, for all the wings studied, Region A stretches from $y/c = 0$ to $y/c \approx 1.3$.

B. Region B

Region B is the region where the spanwise pressure gradient advances separation. It starts at the end of Region A and extends until the effects of the wingtip vortex become dominant. The α_s drops gradually as we move towards the tip.

C. Region C

Region C denotes the region affected by the presence of the wingtip vortex. In this region, α_s drop is sharper than in Region B. Region C is ignored in this work, and the α_s variation in this region is extrapolated from the variation in Region B. Region C was observed to span from 80% of the semi-span to the wingtip.

D. Two-part linear fit

The variation of α_s with spanwise location can be simplified by approxmating it to linear fits in regions A and B, as shown in Figure 9.
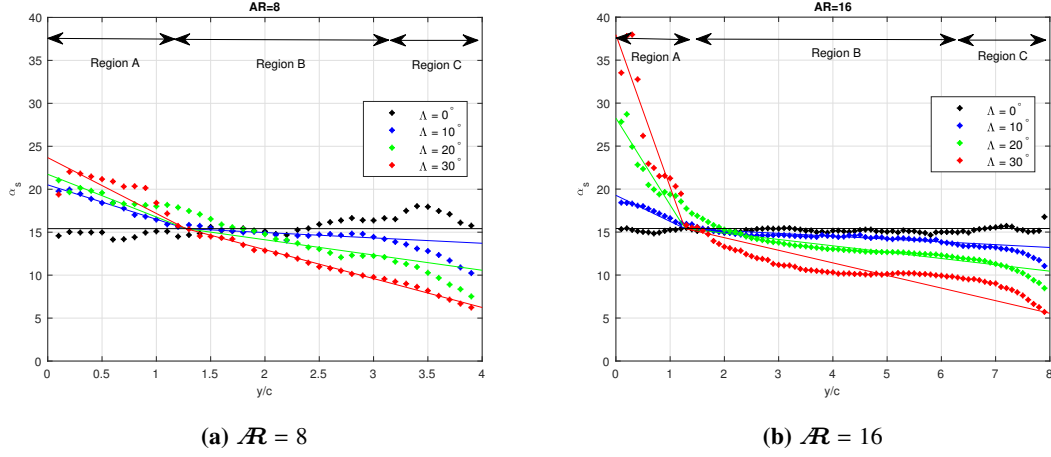

(a) $A\!R = 8$

(b) $A\!R = 16$

**Fig. 9   Spanwise variation of α_s for $\Lambda = 0°, 10°, 20°,$ and $30°$ swept wings**

E. Aspect ratio comparison

Comparing the α_s variations of wings with same sweep but different aspect ratios, it is apparent that in region A, the wings with higher aspect ratio have higher values of α_s. Figure 10 also shows that, regardless of aspect ratio, Region A ends at approximately the same y/c value. In region B, a steeper drop in α_s is observed for the smaller-aspect-ratio wing. We also observe that the α_s decreases to approximately equal values at the tips for wings of equal sweep. Using this observation, we can plot only Region B for all wings, non-dimensionalized by the span of region B, to remove the effect of aspect ratio on the variation of α_s in this region (Figure 11a). The slopes of the linear fits in Region B vary more or less linearly with sweep, as shown in Figure 11b. This information can be used to predict the separation behavior in Region B of swept wings of arbitrary aspect ratio.

(a) $\Lambda = 0$

(b) $\Lambda = 10$

(c) $\Lambda = 20$

(d) $\Lambda = 30$
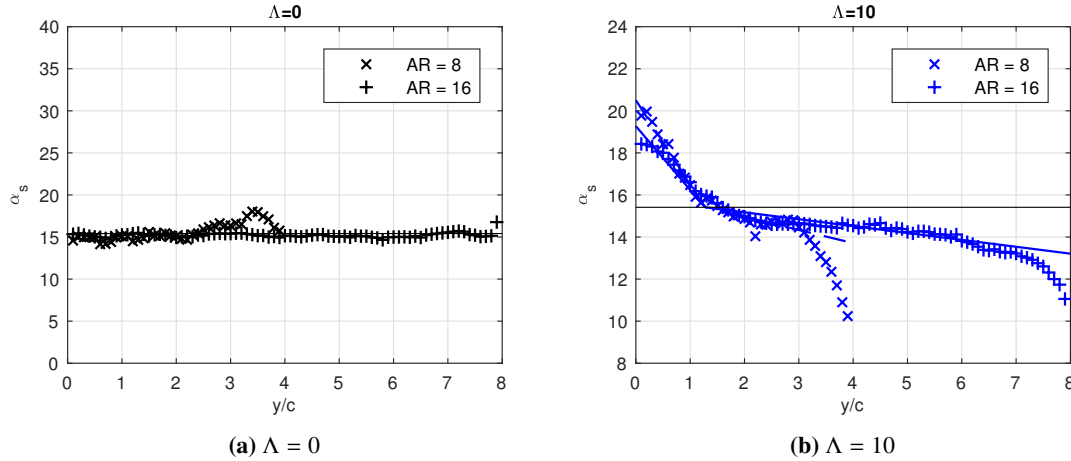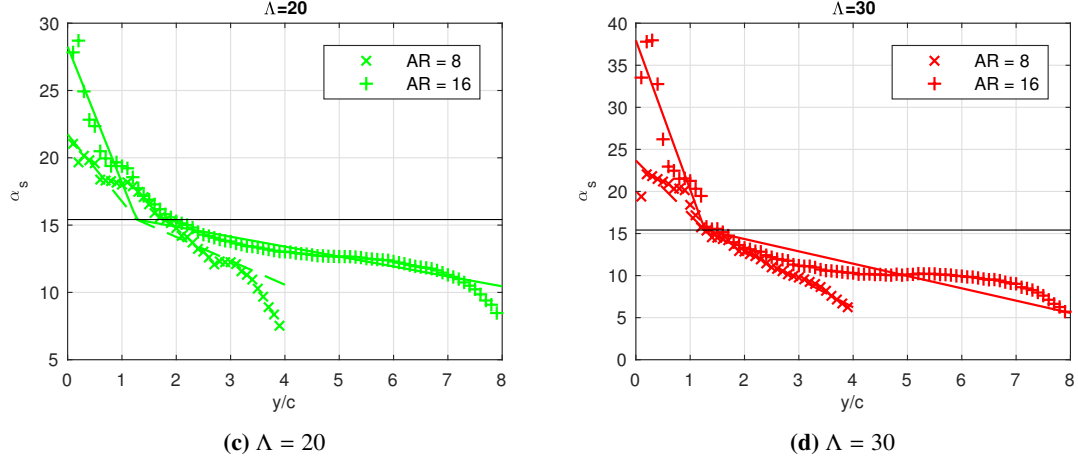
Fig. 10 Spanwise variation of α_s for $AR = 8$ and 16 wings. Black line denotes α_s of the rectangular wing

(a)

(b)
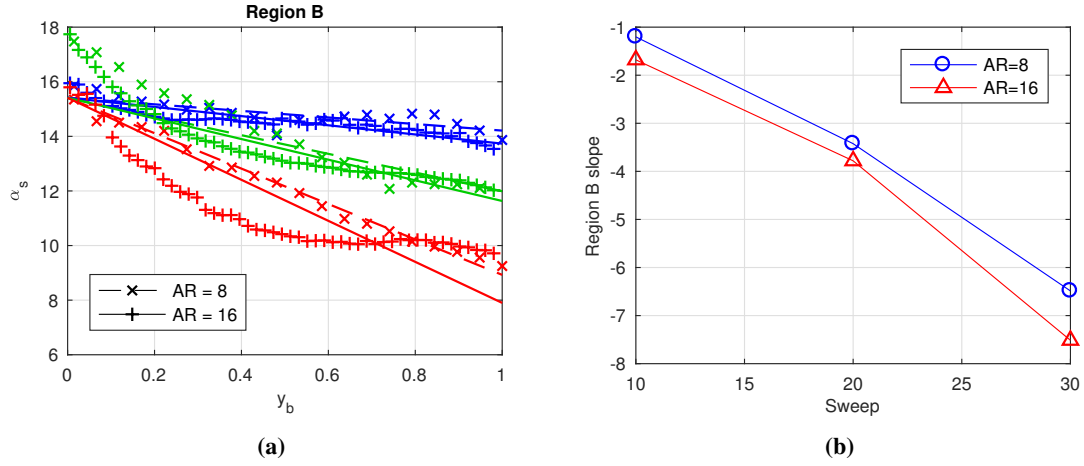
Fig. 11 (a) α_s variation in Region B, isolated and non-dimensionalized by the span of region B, and (b) Slopes of Region B fits

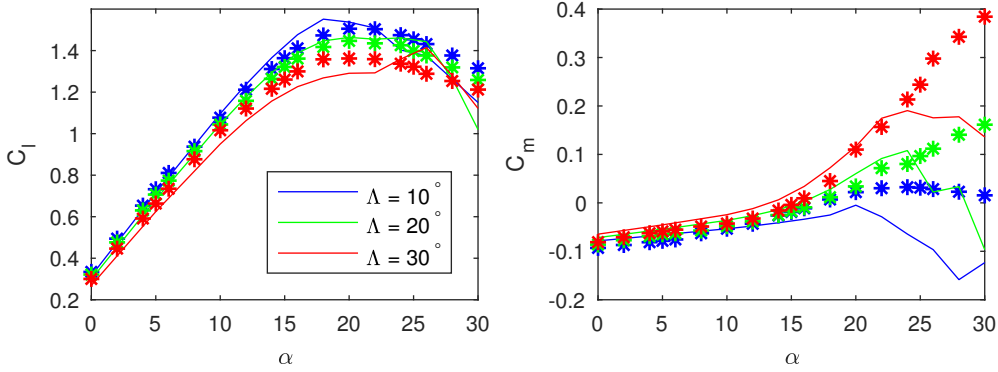## VI. Results from the Low-Order Method

The trends described in the previous section were used to generate the section characteristic curves for the wings studied. These section characteristics were used with the decambering method to obtain wing lift and moment behavior for pre- and post-stall angles of attack. This section presents the results from the low-order method using these characteristics. C_L and C_M vs. α plots for wings of three aspect ratios are presented: $AR = 8$ and 16, for which full CFD solutions were used to obtain section characteristics, and $AR = 12$, for which CFD solutions were used only to compare total lift and moment results with the low-order method. For each aspect ratio, three sweep angles (10, 20, and 30 degrees) are presented.

A. $AR = 8, 16$

For the $AR = 8$ and $AR = 16$ wings, the two-part-linear fits obtained before and shown in Figure 9 were used to generate the section characteristics.

Figures 12 and 13 show the C_L and C_M vs α variation from CFD and the low-order method for the $AR8$ and 16 wings respectively. The C_L predictions from the decambering method match CFD solutions well for the angles of attack considered. Predictions for C_M are also acceptable at lower angles of attack, but the decambering method does not

correctly capture the drop in C_M for $\alpha > 20°$.

Fig. 12 **Comparison of lift and moment about aerodynamic center from the low-order method (*) and CFD (-) for the $\mathcal{R} = 8$ wings**
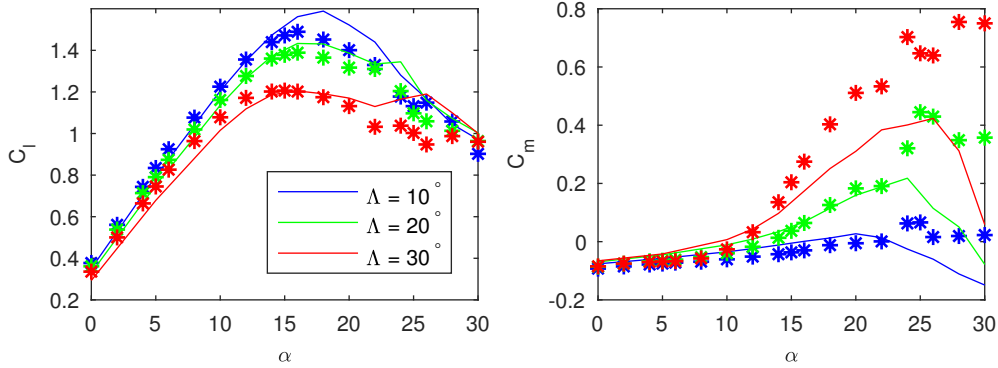
Fig. 13 **Comparison of lift and moment about aerodynamic center from the low-order method (*) and CFD (-) for the $\mathcal{R} = 16$ wings**

B. $\mathcal{R} = 12$

The section characteristics for region B of the $\mathcal{R} = 12$ wings were generated using the observations made in Section V.E. Unfortunately, no such simplification was found for Region A. The behavior in Region A for the $\mathcal{R} = 12$ wings was estimated as halfway between the $\mathcal{R}8$ and $\mathcal{R}16$ behavior. Figure 14 compares low-order predictions with CFD solutions. Again, the lift predictions match CFD solutions well, but the moment predictions beyond $\alpha = 20°$ are not adequate.

VII. Other geometries

The method presented above can be applied to arbitrary wing planforms. This is demonstrated using the partially-swept planform shown in Figure 15a. The wing consists of a rectangular portion of $\mathcal{R} = 4$ from root to $y/c = 2$, and a $30°$ swept portion of $\mathcal{R} = 8$ from $y/c = 2$ to $y/c = 6$. The aspect ratio of the wing is 12.

The α_s variation across the span, obtained using the procedure discussed previously, is shown in Figure 15b. The α_s for the rectangular part is modeled well by the single linear fit for the rectangular wings discussed previously. The swept region can now be divided into an inboard and outboard region. The lower α_s in the outboard region indicates advanced separation. In this region, the α_s variation closely resembles the variation in Region B of the $\mathcal{R} = 8, \Lambda = 30°$ wing. In the inboard region, the tendency for delayed separation is seen from a higher α_s. The slope of the linear fit in this region is greatly reduced in comparison to the corresponding swept wing due to the presence of the rectangular portion of the
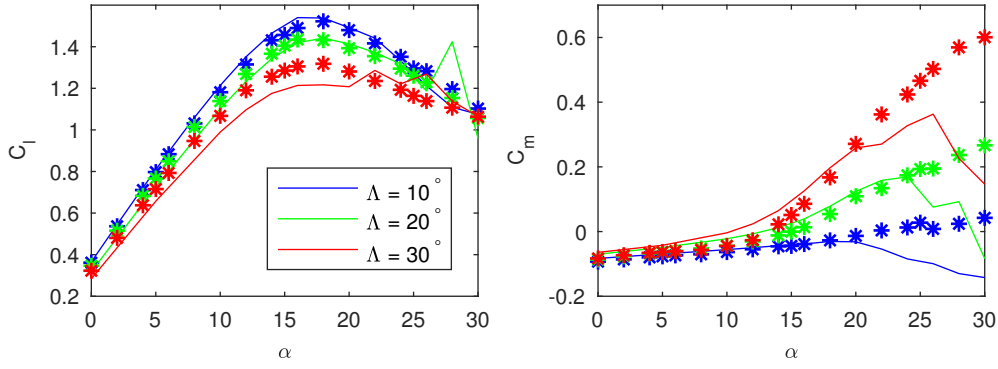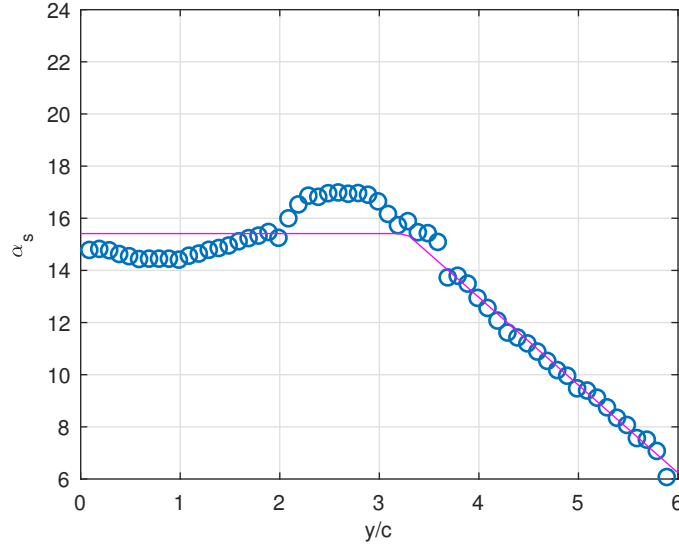
Fig. 14 Comparison of lift and moment about aerodynamic center from the low-order method (*) and CFD (-) for the $\mathcal{R} = 12$ wings

wing. Additionally, the inboard region of the swept portion has the same span ($y/c \approx 1.3$) as Region A of the swept wing.
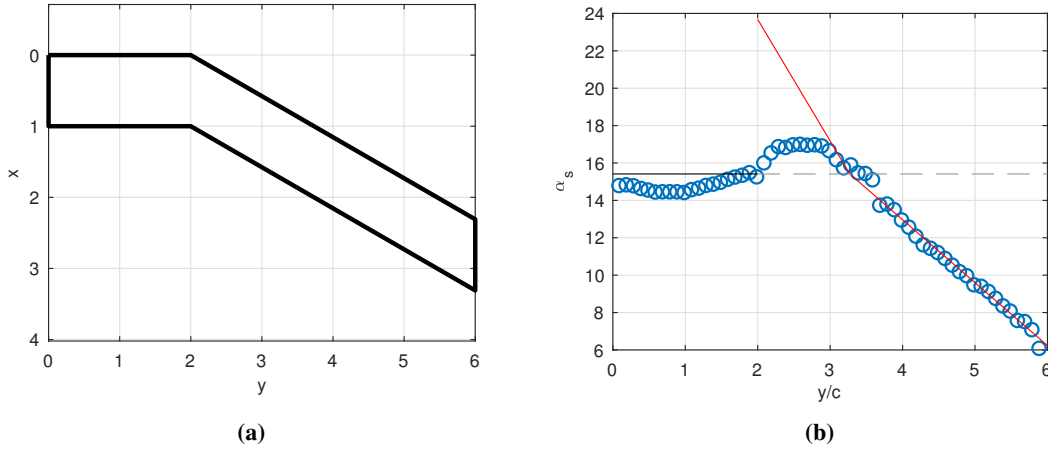

Fig. 15 (a) The partially swept planform (b) α_s variation with y/c for this planform

A test two-part linear fit was created for this wing by combining the fits for the rectangular wing and the 30° -swept $\mathcal{R}8$ wing. The linear fit is shown in Figure 16. Characteristic curves for the sections were generated using this fit, and used in the low-order method. The C_L and C_M vs α predictions from the decambering method are compared with CFD solutions in Figure 17. The lift predictions match the CFD solution very well, but moment predictions become increasingly erroneous for $\alpha > 10°$.

12

Fig. 16   Two-part linear fit used for the partially swept wing
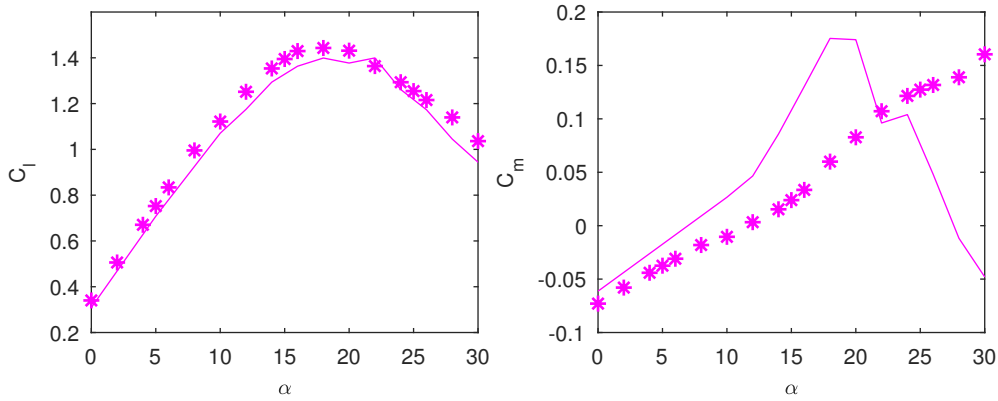
Fig. 17   Comparison of lift and moment about aerodynamic center from the low-order method (*) and CFD (-) for the partially swept wing

VIII. Conclusions

A previously developed methodology to model the spanwise separation behavior of swept wings was applied to wings of differing aspect ratios. Three regions were identified based on the section separation behavior in comparison to the behavior of a rectangular-wing section. Trends in the variation of the quantity α_s with spanwise location and sweep in these regions agree with the trends seen in previous work. It was observed that the region of root influence, characterized by delayed separation, ends at similar spanwise locations, regardless of aspect ratio or sweep. In addition, a method was presented to eliminate the dependence of α_s on aspect ratio, which enables us to predict the characteristics of wings of arbitrary aspect ratios. When these characteristics are used in the decambering method, excellent results are obtained for the wing lift coefficient. Predictions from the low-order method for moment coefficient are good at low angles of attack, but the drop in moment at higher angles of attack ($\geq 20°$) is not captured correctly. Finally, the methodology was applied to a partially swept wing. The behavior of α_s in the outboard swept portion of the wing was unaffected by the rectangular portion. A test fit generated by combining the fits of the rectangular and $Æ\!R8$ $30°$ swept wing was used to obtain low-order results. Good agreement was seen with CFD solutions for the C_L variation. The results in this paper show that the current modeling of stall behavior of swept wings has promise. Additional CFD studies with wings have different planforms and airfoils are planned to further develop the current method.

13

IX. Acknowledgements

References

[1] Sivells, J. C., and Neely, R. H., "Method for Calculating Wing Characteristics by Lifting-Line Theory Using Nonlinear Section Lift Data," NACA TN 1269, April 1947.

[2] Hunton, L. W., and James, H. A., "Use of Two-Dimensional Data in Estimating Loads on a 45-degree Sweptback Wing with Slats and Partial-span Flaps," NACA TN 3040, National Advisory Committee for Aeronautics, Ames Aeronautical Laboratory, Moffett Field, CA, November 1953.

[3] Tseng, J. B., and Lan, C. E., "Calculation of Aerodynamic Characteristics of Airplane Configurations at High Angles of Attack," NASA CR 4182, 1988.

[4] McCormick, B. W., "An Iterative Non-Linear Lifting Line Model for Wings with Unsymmetrical Stall," *SAE Transactions Paper No. 891020*, 1989, pp. 91–98.

[5] van Dam, C. P., Kam, J. C. V., and Paris, J. K., "Design-Oriented High-Lift Methodology for General Aviation and Civil Transport Aircraft," *Journal of Aircraft*, Vol. 38, No. 6, 2001, pp. 1076–1084.

[6] Mukherjee, R., and Gopalarathnam, A., "Poststall Prediction of Multiple-Lifting-Surface Configurations Using a Decambering Approach," *Journal of Aircraft*, Vol. 43, No. 3, 2006, pp. 660–668.

[7] Gallay, S., and Laurendeau, E., "Nonlinear Generalized Lifting-Line Coupling Algorithms for Pre/Poststall Flows," *AIAA Journal*, Vol. 53, No. 7, 2015, pp. 1784–1792. doi:10.2514/1.J053530, URL http://dx.doi.org/10.2514/1.J053530.

[8] Dias, J. N., "Nonlinear Lifting-Line Algorithm for Unsteady and Post-stall Conditions," AIAA Paper 2016-4164, 2016.

[9] Paul, R. C., and Gopalarathnam, A., "Iteration Schemes for Rapid Post-Stall Aerodynamic Prediction of Wings Using a Decambering Approach," *International Journal for Numerical Methods in Fluids*, 2014.

[10] Harper, C. W., and Maki, R. L., "A Review of the Stall Characteristics of Swept Wings," NASA TN D-2373, 1964.

[11] Hosangadi, P., Paul, R., and Gopalarathnam, A., "Improved Stall Prediction for Swept Wings Using Low-Order Aerodynamics," AIAA Paper 2015-3159, Jun. 2015.

[12] Petrilli, J., Paul, R., Gopalarathnam, A., and Frink, N., "A CFD Database for Airfoils and Wings at Post-Stall Angles of Attack," AIAA Paper 2013-2916, June 2013.

[13] Narsipur, S., Gopalarathnam, A., and Edwards, J. R., "Low-Order Modeling of Airfoils with Massively Separated Flow and Leading-Edge Vortex Shedding," AIAA Paper 2018-0813, 2018.